Towards an ultra-long lifespan Li-CO_2: electron structure and charge transfer pathway regulation on hierarchical architecture

Yangyang Wang [a], Jing Wang [a], Jinming Wang [a], Meng Yang [a], Guodong Zou [a,*], Lanjie Li [b], John S. Tse [c], Carlos Fernandez [d], Qiuming Peng [a,*]

[a] State Key Laboratory of Metastable Materials Science and Technology, Yanshan University, Qinhuangdao, 066004, P.R. China

[b] Chengde Iron and Steel Group Co., Ltd, HBIS Group Co., LTD., Chengde, Hebei 067102, China

[c] Department of Physics, University of Saskatchewan, Saskatoon, SK, S7N5B2, Canada

[d] School of Pharmacy and Life Sciences, Robert Gordon University, Aberdeen, AB107GJ, United Kingdom

*Corresponding Authors: zouguodong@ysu.edu.cn, pengqiuming@ysu.edu.cn

Abstract

Lithium-CO_2 batteries are recognized as an essential strategy for efficient carbon sequestration and energy storage to achieve carbon neutrality. Their cycle-ability and polarization voltage, however, are hindered by high decomposition voltage (≈ 4.3-4.5 V) of insulating Li_2CO_3. Herein, we report a significant advance toward the rational design of self-supporting and ultra-long cycle lifetime cathode for Li-CO_2 batteries, dependence on a favorable hierarchical architecture and rich charge transfer constructed by homogeneously distributed MnO_2 nanoplates rooted in the MXene surface supported by carbon paper. Detailedly, it exhibits impressive ultra-long-term stability of 1087 cycles (4348 h) with a low polarization gap (≈ 0.47 V) at a high current of 200 μA cm^{-2}, which is outperformed by all the liquid electrolyte-based Li-CO_2 batteries reported previously. Electronic structure analysis reveals that facile charge transfer occurs between catalytic surface and Li_2CO_3, springing from the -OH functional group (in MXene) to MnO_2 by -OH···O hydrogen bonds, which acts as charge transfer channels, improving the metallicity of Li_2CO_3 and facilitating its decomposition and extending battery cyclability. This work paves an effective trajectory for the future development of highly efficient cathodes for durable metal-CO_2 batteries.

Keywords: MXene; Li-CO_2 batteries; catalyst; ultra-long lifespan; low overpotential

1. Introduction

Energy shortage and environmental pollution are severe challenges for achieving sustainable development of human society [1, 2]. Li-CO_2 batteries offer particularly attractive merits in combination with CO_2 fixation and energy storage [3, 4], in which it shows a coming win-win blueprint by utilizing greenhouse gas (CO_2) as fuel, to alleviate energy shortage and global warming issues [5, 6]. In addition, it is also considered to be one of the most promising beyond Li-ion technologies, with a theoretical energy density of 1876 Wh kg^{-1} [7], far exceeding that of Li-ion batteries (≈ 265 Wh kg^{-1}) [8]. Evidently, the most common reaction mechanism of Li-CO_2 batteries is associated with the formation of lithium carbonate (Li_2CO_3) through a four-electron reaction: $4Li^+ + 3CO_2 + 4e^- \leftrightarrow 2Li_2CO_3 + C$, ($E_o$ = 2.80 V *vs* Li/Li^+) [9], during the CO_2 reduction reaction/CO_2 evolution reaction (CRR/CER) process [10]. Unfortunately, Li_2CO_3 is a wide band gap insulator, leading to sluggish kinetics for its decomposition during the CER process (a high charge voltage up to 4.30 V *vs* Li/Li^+) [11]. Such a high charge potential accelerates both electrode oxidation and electrolyte decompositions [12]. The accumulation of solid carbonate species on the cathode surface, relative to incomplete decomposition or irreversible formation of Li_2CO_3, results in a distinct decrease of space and active sites, further leading to problems such as high polarization gap, poor cycle stability and "sudden death" [13].

It is therefore highly urgent to develop compatible electrode materials to boost their lifespan and reduce polarization voltage by facilitating the reversible formation/decomposition of Li_2CO_3 during the discharge/charge processes [14]. There are several pathways to tailor the decomposition behavior of Li_2CO_3 in the past decade. Firstly,

the decomposition of Li_2CO_3 can be promoted by chemically bonding the catalysts or changing the stable triangular structure of the carbonate[15]. Secondary, to promote decomposition, the discharge product Li_2CO_3 with small particle size or thin-film morphology is also desirable [5, 16, 17]. Thirdly, highly stable amorphous intermediate discharge product $Li_2C_2O_4$ on Li_2CO_3 can enhance battery cycle efficiency [18, 19]. Finally, the increment of the specific surface area of the cathode catalyst would induce uniform nucleation or decomposition of discharge products [20-23]. Although the electrochemical properties of Li-CO_2 batteries are improved greatly, the cyclability is still far beneath the industrial threshold [24].

Theoretically, the increment of the conductivity of Li_2CO_3, from insulator-to-metal transition, will accelerate the decomposition process and hamper its congestion. So, a favorable catalyst is required to own an abundance of itinerant electrons, which stimulates charge transfer from the catalyst surface to Li_2CO_3, perturbing its electron distribution, realigning bond energy and reducing the crystallinity of lithium carbonate[15, 25]. One attractive option to improve the electrical conductivity of catalysts is to develop hybrid materials by combining metal oxides/hydroxides with conductive materials [26, 27]. MnO_2 has been investigated as electrode materials for additional advantages of low cost, environmental friendliness, and extraordinary redox chemistry catalytic activity [28, 29]. Transition-metal carbides and carbonitrides, which are known as MXenes with excellent metal conductivity [30-32], are featured with abundant -F, -OH, or -O functional groups generated during the etching process [33], which can act as active “bridge” to fasten combination with other materials and modulate electronic state [34, 35]. Therefore, a

rational design of a hierarchical architecture wherein the MnO_2 grown and rooted on the surface MXene to adjust surface electron state and change the electrical conductivity of Li_2CO_3, accelerating its decomposition and prolonging the cycling performance.

In present work, we put forward a self-assembly and microwave strategy to facilitate the preparation of cathode layered microstructures (denoted as CPM-MnO_2) for Li-CO_2 batteries, where carbon paper (CP) acts as the 1D substrate and inner core, MXene as the internal dielectric layer, and MnO_2 as the catalyst and antioxidant outer coating. Convincingly, facile charge transfer from the surface of CPM-MnO_2 to Li_2CO_3 by hydrogen bonds improves the conductivity of the latter, benefiting the redox reaction of Li_2CO_3. As a result, CPM-MnO_2 cathode in Li-CO_2 batteries displays an ultra-long-term stability of 1087 cycles (4348 h) with a low polarization gap (≈ 0.47 V) at a high current of 200 μA cm^{-2}, which, to our best knowledge, outperforms available recorded liquid electrolyte-based Li-CO_2 batteries reported hitherto.

2. Experimental Section

2.1 Synthesis of $Ti_3C_2T_x$ MXene dispersion

Delaminated $Ti_3C_2T_x$ suspension was synthesized similarly to our previous method. In detail, 1.6 g LiF was added into 20 mL 9 M HCl under continuous stirring, and 1 g Ti_3AlC_2 was slowly added to the solution. The mixture was stirred at 400 rpm at 35 °C for 24 h. Then the product was rinsed using deionized water several times until the pH of the supernatant was approximately 6. Further, the precipitate was diluted to 200 mL of deionized water and the black mixture was bath sonicated in ice for 1 h. Finally, the solution was centrifuged at 3500 rpm for 10 min to collect the single or few-layered MXene dispersion. The

concentration of this suspension was 5 mg mL^{-1}.

2.2 Fabrication of freestanding CPM-MnO_2 film composites

Firstly, fresh Carbon Paper (CP) was successively treated in the mixture of concentrated sulfuric acid and concentrated nitric acid (V:V =3:1) at 70 °C for 3 h in order to remove the oxide films and impurities on the surface. Next, the processed CP (2*6 cm^2) was immersed in a MXene solution with ultrasound for 1.0 h. The CPM-0.1MnO_2 film was prepared by a microwave-assisted method (MS, XH-8000, Beijing XiangHu Science and Technology Development Co., Ltd., China). Then, the dried CPM was immersed in 50 mL $KMnO_4$ (0.1g) solution and heated to 90 °C at a heating rate of 10 °C min^{-1}, and kept for 15 min with a power of 600W. Ultimate, the CPM-0.1MnO_2 was acquired under vacuum at 60 °C for 24 h. The other different qualities of $KMnO_4$ (0.05 and 0.2g) have also been used to investigate, and the products were designated as CPM-0.05MnO_2, CPM-0.2MnO_2, respectively. CP-0.1MnO_2 is synthesized in the same way as CPM-0.1MnO_2, except without the addition of MXene.

2.3 Material characterization

The phase purity and crystal structure of the samples were recorded on an X-ray diffractometer (Rigaku D/MAX-2005/PC) using Cu Ka radiation (λ=1.5406 Å) with a step scan of 0.02 degree per step and a scan rate of 3 degree/min. SEM was conducted with a Hitachi S-4800. Transmission electron microscope (TEM) images were observed on a Titan ETEM G2 at 300 kV. The specific surface areas and pore size distribution were measured by a Micromeritics ASAP2020 using nitrogen gas adsorption at 77 K (-196°C). X-ray

photoelectron spectroscopy (XPS) were conducted on a ThermoFisher with Al Kα (1486.71 eV) X-ray radiation (15 kV and 10 mA). The binding energies obtained in the XPS analysis were corrected by referencing the C 1s peak position (284.80 eV).

2.4 Electrochemical measurements

Due to the low capacity of Ti_3C_2 film-based Li-CO_2 battery, the current density and specific gravimetric capacity of all electrodes were calculated based on the mass of the MnO_2. The mass loading of the catalyst on each cathode was about 0.30 ± 0.05 mg cm^{-2}. The CR2032 coin-type Li-CO_2 battery composed of a Li foil anode, a glass fiber filter separator, an electrolyte, and an air cathode, were assembled in an argon-filled glove box with an environment of water and oxygen levels less than 0.1 ppm. The galvanostatic discharge/charge tests were collected on a LAND CT2001A battery test instrument. CVs were conducted on a BioLogic VMP3 electrochemical workstation in the potential window of 2.0-4.5 V, and the scan rate was 0.2 mV s^{-1}. EIS curves were carried out on a BioLogic VMP3 system with the typical frequency range from 100 kHz to 10 mHz and a 5mV voltage amplitude.

2.5 Calculations

The DFT calculations were conducted using VASP [36], based on the projector augmented wave (PAW) method [37]. A 4×4 supercell of MnO_2 single layer and MXene with a vacuum of 15Å along c axis were simulated. The PBE exchange-correlation functional within the generalized gradient approximation (GGA) is employed. The cutoff energy of the kinetic energy is 500eV. The k-mash in the Brillouin zone was 3×3×1 *via* Monkhorst-Pack

method [38]. The energy convergence tolerance and force certifications are 1.0×10^{-5}eV/atom and 0.01eV/Å, respectively. The van der Waals (vdW) interaction was involved *via* the semi-empirical DFT-D2 field method [39]. The adsorption energy (ΔE_{ads}) was calculated as follows:

$$\Delta E_{ads} = E_* - (E_{slab} + E_X) \quad (1)$$

where E_* and E_{slab} were the total energy of the specified surface with/without adsorbates, E_X was the total energy of the adsorbates.

The overall chemical reactions for generating Li_2CO_3 were described as

$$2Li(s) + 3/2\ CO_2\ (g) \rightarrow Li_2CO_3(s) + 1/2\ C(s) \quad (2)$$

The change of the free energy (ΔG) in the reaction was calculated considering zero point energy corrections (ZPE) and entropy change ($T\Delta S$) from the vibrational frequencies associated with the normal modes in the harmonic approximation. The entropy of CO_2 molecules under standard conditions (T=298 K) is 213.795 J K^{-1} mol^{-1} taken from the NIST database, and the calculation of CO_2 ($T\Delta S$) is thus 0.66 eV. As a result, the standard Gibbs free energy (ΔG) calculated was -5.76 eV for Li_2CO_3.

3. Results and Discussion

3.1 Characterization of CPM-MnO_2

The hierarchical CPM-MnO_2 composite was synthesized by self-assembly and microwave-assisted process (details are referred to the experimental section), which can be directly used as the cathodes of Li-CO_2 batteries and promote abundant charge transfer through -OH···O hydrogen bonding between MXene and MnO_2, thus reducing the free energy of lithium carbonate decomposition **(Scheme 1)**. Specifically, dependent on

selectively etching the Al layer in Ti_3AlC_2 with LiF/HCl, MXene nanosheets with an average lateral size of several hundred nanometers were firstly obtained **(Fig. S1a-b)**. Subsequently, the positively charged CP treated with the acid was wrapped by MXene with an electronegative surface (Marked as CPM) as evidenced by a strong characteristic peak of (002) at lower angle (2θ≈ 6.5) [40] (**Fig. 1a**). Finally, the Mn^{7+} was reduced to MnO_2 nanosheets with microwave-assisted in the $KMnO_4$, which are evenly dispersed on the surface of MXene (**Fig. 1b-c**). Meanwhile, the major diffraction peaks at about 12.5°, 25.2°, and 37.3° correspond to (001), (002), (-111), planes of δ-MnO_2 (JCPDS No. 80-1098) in CPM-0.1MnO_2, respectively [41, 42]. The cross-sectional scanning electron microscope (SEM) image in **Fig. 1d** shows the interconnected CPM-0.1MnO_2 displays well-defined gradient morphology and the energy-dispersive spectroscopy (EDS) elemental mapping **(Fig. S1c-d and S1e-f)** gives a direct view of the layered distribution of C (55 wt%), Ti (11 wt%), O (16 wt%) and Mn (18 wt%) elements. The transmission electron microscope (TEM) image **(Fig. 1e)** reveals the MnO_2 nanoplates with a length sizes of ~ 100 nm are robustly coupled to MXene growth substrate owing to its ultra-thin feature of several nanometers, which effectively enhances the overall metal abundance of the catalyst [43]. Furthermore, **Fig. 1f** demonstrates that the bandwidth of the MnO_2 nanosheets is ~ 4 nm, and the local high-resolution TEM (HRTEM) image confirms that the distance of lattice fringes of 0.25 and 0.23 nm is assigned to the (200) and (003) planes of the MnO_2, respectively [44].

The surface chemical bonding states of the samples have been probed by X-ray photoelectron spectroscopy (XPS). From comparing the XPS survey of reference materials, the characteristic peaks of Ti 2p, O 1s, C 1s, F 1s, and Mn 2p are observed in CPM-0.1MnO_2

(**Fig. S2a**). The high-resolution XPS Ti 2p spectra in the CPM-0.1MnO_2 (**Fig. S2b**) show that the binding energy of Ti is relative to the conventional characteristics of MXene. It can be seen that the peaks related to Ti-O bonds in CPM-0.1MnO_2 are significantly stronger than those of the original MXene, while the Ti-C bond-related peaks are significantly weaker than those of MXene. It is mainly associated with the partial oxidation of the MXene surface during the synthesis of the composite and the loading effect of MnO_2 [45, 46]. As shown in **Fig. 1g**, both CP-0.1MnO_2 and CPM-0.1MnO_2 exhibit two multiplet-splitting peaks, with a binding energy separation of 11.8 eV between the peaks, which corresponds to the δ-MnO_2 [47]. Notably, the peaks of Mn 2p and O 1s (**Fig. S2c)** of CP-0.1MnO_2 and CPM-0.1MnO_2 have a slightly positive shift by 0.4 and 0.25 eV towards the higher binding, revealing the strong interfacial electron interaction and hydrogen bonds between MnO_2 and MXene.[43] In addition, CPM-0.1MnO_2 possess obvious absorption peaks of -OH (3410 cm^{-1}) and C=O (1650 cm^{-1}) (FTIR, **Fig. 1h**), covered by MXenes [48], and a shoulder peak of the O-H stretching band at 1350 cm^{-1} with its peak shifted to short wavenumber, indicating it can form strong hydrogen bonds with MXene and MnO_2 [49]. Here, when the MXene mixed with MnO_2 nanosheets, the outward-facing -OH groups on the surface of MXene can formed the -OH···O hydrogen bonds with MnO_2 nanosheets, which enhances the interaction between these two types of nanosheets [50, 51].

This structure is further confirmed by the Raman spectra (**Fig. S2d**). Compared with CP, MXene and MnO_2, except for the pristine D bond (around 1350 cm^{-1}, the disordered defects) and G band (around 1600 cm^{-1}, the graphitic carbon bonds) [52], the new peaks of both MXene (557 cm^{-1}) [53] and MnO_2 (637 cm^{-1}) [54] are detected in the CPM-0.1MnO_2,

indicating the successful loading of MXene (3 wt%) and MnO_2 (8 wt%) onto CP (89 wt%). The physical properties have been also investigated by nitrogen adsorption and desorption test. Compared with other electrodes, the CPM-0.1MnO_2 has a larger Brunauer-Emmett-Teller (BET) specific surface area (19.66 m^2 g^{-1}, **Fig. S2e**), which offers more active sites for CO_2 in the charging and discharging processes. Additionally, the pore structure of CPM-0.1MnO_2 is predominantly mesoporous, with a void size of 2.3-3.6 nm (**Fig. S2f)**, corresponding to the IV isotherm type at 77 K.

In addition, to investigate the effect of cathode catalyst content and conductivity on the cycling performance of the battery, we prepared MnO_2 with different concentrations (termed as CPM, CPM-0.05MnO_2 and CPM-0.2MnO_2). They show the similar morphologies (**Fig. S3)**. In contrast, the MXene dopant can improve the conductivity of CP-MnO_2 (**Fig. S4)**. Basically, the conductivity is negatively dependent on the co-doping concentration and its conductivity decreases with the increase of co-doping concentration [26].

3.2 Electrochemical Properties

Fig. 2a presents the cyclic voltammetry (CV) response of batteries at a constant scan rate of 0.2 mV s^{-1} within 2.0-4.5 V. It is noted that the battery with the CPM-0.1MnO_2 cathode exhibits highest reduction onset potential (2.93V, CRR) and lowest oxidation onset potential (3.82V, CER), suggesting the highest catalytic activity of CPM-0.1MnO_2 cathode compared to those of CPM and CP-0.1MnO_2 cathodes. More attractively, the CPM-0.1MnO_2-based batteries show the lowest polarization gap 0.47 V as compared to those of the CP- (1.75 V), CPM- (1.0 V) and CP-0.1MnO_2-based (0.9 V) batteries during the first cycle (**Fig. S5**).

The Li-CO_2 battery was found to cycle up to 1087 consecutive discharge and charge cycles with a capacity of 400 μA h cm^{-2} per cycle at a current density of 200 μA cm^{-2} (**Fig. 2b**).. The first cycle discharge voltage is 2.65 V, which remains to be 2.48 V in 1087^{th} cycle, only 6% lose in the discharge potential. Correspondingly, the increment of charge potential is also as small as 7% after 1087 cycles, further confirming the stable and sustainable performance of the cell during continuous cycles. To investigate the sloping feature of the curves, a CPM-0.1MnO_2 electrode tested in Ar within a 2.0-4.2 V (**Fig. S6**) diliveries a reversible capacity of $\approx$ 70 μA h cm^{-2} and an average voltage of $\approx$ 3.01 V after three cycles activation at 200 μA cm^{-2}. The lithium-ion insertion capacity accounts for $\approx$ 17.5% of the total capacity, which causes the high voltage plateau as well as the sloping feature[55].

We also tested the rate capability of the Li-CO_2 battery at different current densities of 40, 80, and 200 μA cm^{-2}, as shown in **Fig. 2c** and **Fig. S7**. The results indicate that the battery shows extreme-low polarization gap (0.43 V) at the current density of 40 μA cm^{-2}, which increases to 0.57 V after 250 cycles (**Fig. 2c**). Polarization gaps of 0.61 and 0.70 V were obtained for higher current densities of 80 and 200 μA cm^{-2} after 250 cycles, respectively, slightly larger than that under the current density of 40 μA cm^{-2}. Note that the overpotential of the cathode maintains at 0.88V after 1087 cycles (**Fig. S7c**).

The voltage-time for the CPM-0.1MnO_2-based battery at a current density of 200 μA cm^{-2} lasts 4348h, *i.e.*, over 181 days (**Fig. 2d)**, suggesting the longest life-span compared with those of CPM- (60 cycles for 240h) and CP-0.1MnO_2-based (400 cycles for 1600h) battery. The ultra-long lifetime and stable cycle numbers of CPM-0.1MnO_2 battery are also superior to other reported materials under similar conditions in the liquid electrolyte-based Li-CO_2

battery (**Fig. 2e and Table S2**). Due to the variation of catalyst content and conductivity, CPM-0.05MnO_2-based and CPM-0.2MnO_2-based batteries were merely run for 189 and 190 cycles respectively, much less than the 280 cycles of the CPM-0.1MnO_2-based battery at 40 μA cm^{-2} (**Fig. S8-9**). In addition, Li-CO_2 batteries based on the CPM-0.1MnO_2 cathode exhibited an excellent rate capability (**Fig. S10**) with remarkable reversibility in the discharge potential upon reducing the current density back to 40 μA cm^{-2}, compared to the CPM and CP-0.1MnO_2. As seen in **Fig. S11**, CPM-0.1MnO_2 exhibited the highest discharge capacity of 4500 μA h cm^{-2}, which is much higher than the corresponding value for CPM (620 μA h cm^{-2}) and CP-0.1MnO_2 (2640 μA h cm^{-2}).

3.3 Reaction Process

Fig. 3a shows typical discharge/charge curves of Li-CO_2 batteries using CPM-0.1MnO_2 as catalyst. The corresponding *ex-situ* XRD, Raman and XPS were used to trace structural changes of discharge product (**Fig. 3b-c and Fig. S12**). Obviously, three emerged peaks located at 21.32°, 30.6°, and 31.8° are observed with the continuously changed peak intensity as discharge/charge states being proceed, which can be identified as the (-110), (-202), (002) planes of Li_2CO_3 (JCPDS No. 22-1141), demonstrating that Li_2CO_3 was the final discharge product, and the reaction was reversible. It is also noticed that, a broad peak located at 1080 cm^{-1} attributable to vibration modes in Li_2CO_3 gradually appeares/disappeares with the proceeding of the discharge/charge [23], and the intensity ratio of the D band and the G band in the discharged state becomes larger (0.86) than that of the pristine condition (0.69), demonstrating the formation of the amorphous carbon [56].

In addition, the *ex-situ* XPS test also confirmed the views mentioned above (**Fig. S12a-b**)

[24, 57]. That is, the C 1s and Li 1s spectra of the product show peaks at 289.8 and 55.2 eV, respectively, corresponding to the formation of Li_2CO_3 [17], which is completely decomposed during the charging process. Notably, the rich charge transfer between MXene and MnO_2 changes the conductivity of the discharge products, resulting in a larger integration area and half-peak width of Li_2CO_3 at the CPM-0.1MnO_2 base than at the CP-0.1MnO_2 base after 200 cycles (**Fig. S12c-d**) [58, 59].

This trend is also confirmed by the EIS measure (**Fig. S13**). Compared with the pristine electrode, a larger semicircle appears at the discharged state, indicating a significantly increased impedance caused by precipitating the insulating Li_2CO_3 on the surface of the CPM-0.1MnO_2 electrode. The original interfacial (high-frequency part), charge transfer (high-middle frequency regions), and diffusion resistances (straight line) can be largely recovered during the subsequent recharging process. Nevertheless, CPM and CP-0.1MnO_2 are not capable of returning to their original state after charging, revealing CPM-0.1MnO_2 enables the lowest charge transfer resistance and the highest conductivity and reversibility.

We also performed the morphology and composition of the discharge product at higher cycles using several techniques. SEM images of the CPM-0.1MnO_2 cathodes (**Fig. 3d-e**) after the 200th cycles indicate a film-like morphology of the discharge products on the cathode surface [17, 18], contributing to the strong connection between Li_2CO_3 and MnO_2 porous flakes，and it completely disappears after the charge experiment. In contrast, the discharge products of CP-0.1MnO_2 and CPM-based batteries are not completely decomposed and the residues are adhered to the catalyst surface (**Fig. S14**). TEM and selected area electron diffraction (SAED) images depicted from the cathode (**Fig. 3f**) show the highly crystalline

MXene, MnO_2 and discharge product (Li_2CO_3)，while the SAED of the surface is used to identify the crystalline MXene. The TEM sample were prepared by physically removing the discharge products from the cathode, causing the film-like product to break up. Therefore, the particles we see are large platelets with crystallites with single crystal domains stretching as far as several 10's of nm [17], consistent with a Li_2CO_3 discharge product that is film-like. The HRTEM analysis (**Fig. 3g**) of discharge products of Li_2CO_3 thin films reveals that the lattice fringe distances of the (-202) and (002) planes are 0.29 and 0.28 nm, respectively, which are consistent with the Li_2CO_3 reference sample.

To further elucidate the growth and ablation process of Li_2CO_3, *in-situ* environmental TEM has been performed to observe the morphology and structure evolution of CPM-0.1MnO_2 during the discharge-charge process. The images of CPM-0.1MnO_2 cathode in **Fig. 3h-j** (**captured from Movie 1**) show Li_2CO_3 gradually grows and increases, with the increment of the discharge time. Subsequently, the surface of the electrode becomes vague and the lithium electrode collapses, due to the simultaneous transport of Li ions. Conversely, as the charging process proceeds, the product gradually disappears, until the electrode surface is as fresh as that of the pristine electrode. The *in-situ* SAED patterns show that the primitive electrode is composed of MXene and MnO_2, and they change to a mixture of MXene, MnO_2, and Li_2CO_3 after discharging. In reverse, the cathode returns to being MXene and MnO_2 after recharging, providing further evidence for Li_2CO_3 formation and decomposition in the reversibility of the Li-CO_2 battery.

In addition, in situ differential electrochemical mass spectrometry (DEMS) (**Fig. S15**) has been employed to detect CO_2 emissions while neither O_2 nor CO signals fluctuate, further indicating that the main product of the charging process is CO_2, validating the operating

mechanism of the CPM-0.1MnO_2-based Li-CO_2 batteries with $4Li^+ + 3CO_2 + 4e^- \leftrightarrow 2Li_2CO_3 + C$. On the other hand, the release voltage platform for CO_2 in the initial stage of CPM-0.1MnO_2 charging is approximately 3.15 V, which is higher than the 2.4 V of CP-0.1MnO_2, demonstrating a better catalytic activity for Li_2CO_3 decomposition.

3.4 Theory Interpretation

To intrinsically unravel the relations between Li_2CO_3 electrical conductivity features and electrochemical performance, charge density distribution, active substance chemisorption as well as Bader charge are investigated. It is found that the adsorption of Li_2CO_3 is stronger for M-MnO_2 (E_{ads} = -6.044 eV, **Fig. 4a**), compared with that of bare MnO_2 (E_{ads} = -5.709 eV, **Fig. 4d**). This can be rationalized by the more charge transfer from the material surface to Li_2CO_3 in M-MnO_2 than that in MnO_2 (**Fig. 4b, e and Fig. S16-17**). As given in **Fig. S18** and **Table S4,** the average Bader charge on O atom in Li_2CO_3 adsorbed on M-MnO_2 is 0.05 eV over that binding on bare MnO_2 surface and Li_2CO_3 with fewer Li-O bonds on the M-MnO_2 surface is susceptible to accelerated decomposition. It reveals that a strong interaction exists between MnO_2 and Ti_3C_2-OH matrix within M-MnO_2 catalyst during the CRR process, manifesting as electron transfer from -OH functional group to O atom by a -OH⋯O hydrogen bond serving as a “highway charge transfer channel” [60, 61]. As a result, it drives the insulator-to-metal transition of Li_2CO_3 on the M-MnO_2 surface (**Fig. 4c, f)**, consistent with the experimental results of XPS (Li1s and C1s, **Fig. S12**)，reducing charging voltage and promoting its decomposing kinetics.

In addition，the free energy profile investigates the possible reaction mechanisms to produce Li_2CO_3 and gradients promoting long-term stability in CPM-0.1MnO_2. The overall reactions [$2Li(s) + CO_2(g) \leftrightarrow Li_2CO_3(s) + C(s)$] that occur under the CO_2 condition in

Li-CO_2 batteries are assumed to obey a two-electron pathway, relative to five reaction pathways (**Table S3**). The calculated standard Gibbs free energy is -5.74 eV for Li_2CO_3, in well agreement with the previous value [19]. In addition, the strong adsorption of adsorbed Li_2CO_3 in M-MnO_2 attains lower Gibbs free energy (-5.74 eV for M-MnO_2 *vs* -5.63 eV for MnO_2, **Fig. 4g-h**), suggesting that it is more facile for M-MnO_2 to produce Li_2CO_3 as the final product. The adsorption of Li_2CO_3 by MXene has also been calculated but some other key reaction intermediates to form Li_2CO_3 are not stable on its surface, underlying that the full free energy change profile can not be accomplished (**Fig. S19**). As shown in **Fig. 4g-h** and **Fig. S20**, the surface of both M-MnO_2 and MnO_2 can easily catch Li and CO_2 to form *Li or *CO_2 intermediates, in view of the downhill step which underlines exothermic reaction. This is consistent with the negative adsorption energy (**Fig. S21-22**). In the following steps, either *$LiCO_2$ or *CO_3 is formed and these steps remain downhill for M-MnO_2. However, they are all uphill for MnO_2, i.e., *Li →*$LiCO_2$, *CO_2→*$LiCO_2$ and *CO_2→*CO_3, hampering the nucleation processes of Li_2CO_3 without external potential. Intriguingly, all the steps afterward for M-MnO_2 attains downhill, which occurs spontaneously in ambient conditions. Furthermore, the decomposition phase in M-MnO_2 (*Li_2CO_3→*$LiCO_3$ or *Li_2CO_3→*Li_2CO_2) requires less energy, which is difficult for bare MnO_2 with larger steps, rationalizing the excellent long-cycle performance and extremely low overpotential observed in experiment.

4. Conclusions

To tackle with the problem of high voltage decomposition of discharge product Li_2CO_3, we successfully synthesized a novel CPM-MnO_2 hierarchical structure for a stand-alone

cathode in Li-CO_2 batteries. Benefiting from the facile charge transfer from the catalytic surface to the discharge product, the rechargeable Li-CO_2 batteries exhibit high electrochemical properties. Operation time and stable cycle numbers are far superior to those of the reported materials under similar conditions in Li-CO_2 batteries. Theoretical analysis demonstrates that charge transfer channels between the catalyst and Li_2CO_3 are formed through the OH...O hydrogen bonds，which change the conductivity of Li_2CO_3 and accelerate decomposition, resulting in high cyclability and low overpotential. Taking into account its simplicity, scalable character and outstanding performance, this hierarchical composite electrode paves a promising shortcut to accelerate the development of Li-CO_2 batteries based on both theoretical and applicable viewpoints.

Declaration of Competing Interest

The authors declare that they have no known competing financial interests or personal relationships that could have appeared to influence the work reported in this paper.

Acknowledgements

We greatly acknowledge the financial support from National Natural Science Foundation-Outstanding Youth Foundation (51971194, 51771162) and Hebei Province Talent project (A201910002) and Top Young Scholars Foundation (BJ2021042), NSF of Hebei province (B2021203016，E2022203167)，Foreign Intelligence Introduction Program of Heibei Province (213000302), the Natural Science Foundation of Hebei Province for Innovation Groups Program (C2022203203), Hebei Postgraduate Innovation Grant Project (CXZZBS2022142). We would like to express our gratitude to the Ministry of Education

Yangtze River scholar Professor Program (T2020124). We would like to express our appreciation to the Gang Huang group for their efforts in supporting DEMS. JST wishes to thank National Science and Engineering Council for a Discovery Grant and Compute Canada for the allocation of computational resources.

Supplementary materials

Supplementary material associated with this article can be found, in supporting information.

References

[1] M. Liu, Y. Pang, B. Zhang, P. De Luna, O. Voznyy, J. Xu, X. Zheng, C.T. Dinh, F. Fan, C. Cao, F.P. de Arquer, T.S. Safaei, A. Mepham, A. Klinkova, E. Kumacheva, T. Filleter, D. Sinton, S.O. Kelley, E.H. Sargent, Enhanced electrocatalytic CO_2 reduction *via* field-induced reagent concentration, Nature 537 (2016) 382-386.

[2] J. Wang, L. Ma, J. Xu, Y. Xu, K. Sun, Z. Peng, Oxygen electrochemistry in Li- O_2 batteries probed by in situ surface- enhanced raman spectroscopy, SusMat 1 (2021) 345-358.

[3] R. Pipes, A. Bhargav, A. Manthiram, Phenyl disulfide additive for solution- mediated carbon dioxide utilization in Li-CO_2 batteries, Adv. Energy Mater. 9 (2019) 1900453.

[4] D. Cao, X. Liu, X. Yuan, F. Yu, Y. Chen, Redox mediator-enhanced performance and generation of singlet oxygen in Li-CO_2 batteries, ACS Appl. Mater. Interfaces 13 (2021) 39341-39346.

[5] C. Li, Z. Guo, B. Yang, Y. Liu, Y. Wang, Y. Xia, A rechargeable Li-CO_2 battery with a gel polymer electrolyte, Angew. Chem. Int. Ed. 56 (2017) 9126-9130.

[6] X. Xiao, W. Yu, W. Shang, P. Tan, Y. Dai, C. Cheng, M. Ni, Investigation on the strategies

for discharge capacity improvement of aprotic Li-CO_2 batteries, Energy & Fuels 34 (2020) 16870-16878.

[7] Z. Zhang, W.L. Bai, Z.P. Cai, J.H. Cheng, H.Y. Kuang, B.X. Dong, Y.B. Wang, K.X. Wang, J.S. Chen, Enhanced electrochemical performance of aprotic Li-CO_2 batteries with a ruthenium-complex-based mobile catalyst, Angew. Chem. Int. Ed. 60 (2021) 16404-16408.

[8] A. Ahmadiparidari, R.E. Warburton, L. Majidi, M. Asadi, A. Chamaani, J.R. Jokisaari, S. Rastegar, Z. Hemmat, B. Sayahpour, R.S. Assary, B. Narayanan, P. Abbasi, P.C. Redfern, A. Ngo, M. Voros, J. Greeley, R. Klie, L.A. Curtiss, A. Salehi-Khojin, A long-cycle-life lithium-CO_2 battery with carbon neutrality, Adv. Mater. 31 (2019) 1902518.

[9] X. Xiao, P. Tan, X. Zhu, Y. Dai, C. Cheng, M. Ni, Investigation on the discharge and charge behaviors of Li-CO_2 batteries with carbon nanotube electrodes, ACS Sustainable Chem. Eng. 8 (2020) 9742-9750.

[10] L. Song, C. Hu, Y. Xiao, J. He, Y. Lin, J.W. Connell, L. Dai, An ultra-long life, high-performance, flexible Li-CO_2 battery based on multifunctional carbon electrocatalysts, Nano Energy 71 (2020) 104595.

[11] X.-X. Wang, G.-J. Ji, P. She, F. Li, Q.-C. Liu, H.-F. Wang, J.-J. Xu, Bio-inspired design of strong self-standing cathode toward highly stable reversible Li-CO_2 batteries, Chem. Eng. J. 426 (2021) 131101.

[12] X. Li, J. Zhang, G. Qi, J. Cheng, B. Wang, Vertically aligned N-doped carbon nanotubes arrays as efficient binder-free catalysts for flexible Li-CO_2 batteries, Energy Storage Mater. 35 (2021) 148-156.

[13] Y. Zhai, H. Tong, J. Deng, G. Li, Y. Hou, R. Zhang, J. Wang, Y. Lu, K. Liang, P. Chen, F.

Dang, B. Kong, Super-assembled atomic Ir catalysts on Te substrates with synergistic catalytic capability for Li-CO_2 batteries, Energy Storage Mater. 43 (2021) 391-401.

[14] X. Li, J. Zhou, J. Zhang, M. Li, X. Bi, T. Liu, T. He, J. Cheng, F. Zhang, Y. Li, X. Mu, J. Lu, B. Wang, Bamboo-like nitrogen-doped carbon nanotube forests as durable metal-free catalysts for self-powered flexible Li-CO_2 batteries, Adv. Mater. 31 (2019) 1903852.

[15] X. Zhang, T. Wang, Y. Yang, X. Zhang, Z. Lu, J. Wang, C. Sun, Y. Diao, X. Wang, J. Yao, Breaking the stable triangle of carbonate *via* W-O bonds for Li-CO_2 batteries with low polarization, ACS Energy Lett. 6 (2021) 3503-3510.

[16] J. Li, H. Zhao, H. Qi, X. Sun, X. Song, Z. Guo, A.G. Tamirat, J. Liu, L. Wang, S. Feng, Drawing a pencil-trace cathode for a high-performance polymer-based Li-CO_2 battery with redox mediator, Adv. Funct. Mater. 29 (2019) 1806863.

[17] M. Asadi, B. Sayahpour, P. Abbasi, A.T. Ngo, K. Karis, J.R. Jokisaari, C. Liu, B. Narayanan, M. Gerard, P. Yasaei, X. Hu, A. Mukherjee, K.C. Lau, R.S. Assary, F. Khalili-Araghi, R.F. Klie, L.A. Curtiss, A. Salehi-Khojin, A lithium-oxygen battery with a long cycle life in an air-like atmosphere, Nature 555 (2018) 502-506.

[18] Y. Xing, Y. Yang, D. Li, M. Luo, N. Chen, Y. Ye, J. Qian, L. Li, D. Yang, F. Wu, R. Chen, S. Guo, Crumpled Ir nanosheets fully covered on porous carbon nanofibers for long-life rechargeable lithium-CO_2 batteries, Adv. Mater. 30 (2018) 1803124.

[19] C. Yang, K. Guo, D. Yuan, J. Cheng, B. Wang, Unraveling reaction mechanisms of Mo_2C as cathode catalyst in a Li-CO_2 battery, J. Am. Chem. Soc. 142 (2020) 6983-6990.

[20] H. Wang, K. Xie, Y. You, Q. Hou, K. Zhang, N. Li, W. Yu, K.P. Loh, C. Shen, B. Wei, Realizing interfacial electronic interaction within ZnS quantum dots/N-rGO heterostructures

for efficient Li-CO_2 batteries, Adv. Energy Mater. 9 (2019) 1901806.

[21] Y. Xiao, F. Du, C. Hu, Y. Ding, Z.L. Wang, A. Roy, L. Dai, High-performance Li-CO_2 batteries from free-standing, binder-free, bifunctional three-dimensional carbon catalysts, ACS Energy Lett. 5 (2020) 916-921.

[22] C. Hu, L. Gong, Y. Xiao, Y. Yuan, N.M. Bedford, Z. Xia, L. Ma, T. Wu, Y. Lin, J.W. Connell, R. Shahbazian-Yassar, J. Lu, K. Amine, L. Dai, High-performance, long-life, rechargeable Li-CO_2 batteries based on a 3D holey graphene cathode implanted with single iron atoms, Adv. Mater. 32 (2020) 1907436.

[23] Y. Mao, C. Tang, Z. Tang, J. Xie, Z. Chen, J. Tu, G. Cao, X. Zhao, Long-life Li-CO_2 cells with ultrafine IrO_2-decorated few-layered δ-MnO_2 enabling amorphous Li_2CO_3 growth, Energy Storage Mater. 18 (2019) 405-413.

[24] Y. Qiao, J. Yi, S. Wu, Y. Liu, S. Yang, P. He, H. Zhou, Li-CO_2 electrochemistry: a new strategy for CO_2 fixation and energy storage, Joule 1 (2017) 359-370.

[25] C. Wang, Y. Lu, S. Lu, S. Ma, X. Zhu, Z. Li, Q. Liu, Boosting Li-CO_2 battery performances by engineering oxygen vacancy on NiO nanosheets array, J. Power Sources 495 (2021) 229782.

[26] B. Ge, Y. Sun, J. Guo, X. Yan, C. Fernandez, Q. Peng, A Co-doped MnO_2 catalyst for Li-CO_2 batteries with low overpotential and ultrahigh cyclability, Small 15 (2019) 1902220.

[27] Y. Hou, J. Wang, J. Liu, C. Hou, Z. Xiu, Y. Fan, L. Zhao, Y. Zhai, H. Li, J. Zeng, X. Gao, S. Zhou, D. Li, Y. Li, F. Dang, K. Liang, P. Chen, C. Li, D. Zhao, B. Kong, Interfacial super-assembled porous CeO_2/C frameworks featuring efficient and sensitive decomposing Li_2O_2 for smart Li-O_2 batteries, Adv. Energy Mater. 9 (2019) 1901751.

[28] J.H. Kim, C. Choi, J.M. Lee, M.J. de Andrade, R.H. Baughman, S.J. Kim, Ag/MnO_2 composite sheath-core structured yarn supercapacitors, Sci. Rep. 8 (2018) 13309.

[29] R. Yang, Y. Fan, R. Ye, Y. Tang, X. Cao, Z. Yin, Z. Zeng, MnO_2- based materials for environmental applications, Adv. Mater. 33 (2021) 2004862.

[30] G. Zou, J. Guo, X. Liu, Q. Zhang, G. Huang, C. Fernandez, Q. Peng, Hydrogenated core-shell MAX@$K_2Ti_8O_{17}$ pseudocapacitance with ultrafast sodium storage and long-term cycling, Adv. Energy Mater. 7 (2017) 1700700.

[31] A. Iqbal, F. Shahzad, K. Hantanasirisakul, M.-K. Kim, J. Kwon, J. Hong, H. Kim, D. Kim, Y. Gogotsi, C.M. Koo, Anomalous absorption of electromagnetic waves by 2D transition metal carbonitride Ti_3CNT_x (MXene), Science 369 (2020) 446-450.

[32] F. Shahzad, M. Alhabeb, C.B. Hatter, B. Anasori, S.M. Hong, C.M. Koo, Y. Gogotsi, Electromagnetic interference shielding with 2D transition metal carbides (MXenes), Science 353 (2016) 1137-1140.

[33] A. VahidMohammadi, J. Rosen, Y. Gogotsi, The world of two-dimensional carbides and nitrides (MXenes), Science 372 (2021).

[34] Z. Hu, Y. Xie, D. Yu, Q. Liu, L. Zhou, K. Zhang, P. Li, F. Hu, L. Li, S. Chou, S. Peng, Hierarchical $Ti_3C_2T_x$ MXene/carbon nanotubes for low overpotential and long-life Li-CO_2 batteries, ACS Nano 15 (2021) 8407-8417.

[35] J. Gu, Q. Zhu, Y. Shi, H. Chen, D. Zhang, Z. Du, S. Yang, Single zinc atoms immobilized on MXene ($Ti_3C_2Cl_x$) layers toward dendrite-free lithium metal anodes, ACS Nano 14 (2020) 891-898.

[36] G. Kresse, J. Furthmuller, Efficient iterative schemes for ab initio total-energy

calculations using a plane-wave basis set, Physical Review B 54 (1996) 11169.

[37] J.P. Perdew, K. Burke, M. Ernzerhof, Generalized gradient approximation made simple, Physical Review Letters 77 (1996) 3865.

[38] H.J. Monkhorst, J.D. Pack, Special points for brillouin-zone integrations, Physical Review B 13 (1976) 5188-5192.

[39] S. Grimme, J. Antony, S. Ehrlich, H. Krieg, A consistent and accurate ab initio parametrization of density functional dispersion correction (DFT-D) for the 94 elements H-Pu, J Chem Phys 132 (2010) 154104.

[40] Y. Jiang, M. Tian, H. Wang, C. Wei, Z. Sun, M.H. Rummeli, P. Strasser, J. Sun, R. Yang, Mildly oxidized MXene (Ti_3C_2, Nb_2C, and V_2C) electrocatalyst *via* a generic strategy enables longevous Li-CO_2 battery under a high rate, ACS Nano 15 (2021) 19640–19650.

[41] S. Liu, Y. Zhu, J. Xie, Y. Huo, H.Y. Yang, T. Zhu, G. Cao, X. Zhao, S. Zhang, Direct growth of flower-like δ-MnO_2 on three-dimensional graphene for high-performance rechargeable Li-O_2 batteries, Adv. Energy Mater. 4 (2014) 1301960.

[42] F.W. Boyom-Tatchemo, F. Devred, G. Ndiffo-Yemeli, S. Laminsi, E.M. Gaigneaux, Plasma-induced redox reactions synthesis of nanosized α-, γ- and δ-MnO_2 catalysts for dye degradation, Appl. Catal. B：Environ. 260 (2020) 118159.

[43] L. Deng, K. Zhang, D. Shi, S. Liu, D. Xu, Y. Shao, J. Shen, Y. Wu, X. Hao, Rational design of schottky heterojunction with modulating surface electron density for high-performance overall water splitting, Appl. Catal. B：Environ. 299 (2021) 120660.

[44] Y. Jin, L. Zou, L. Liu, M.H. Engelhard, R.L. Patel, Z. Nie, K.S. Han, Y. Shao, C. Wang, J. Zhu, H. Pan, J. Liu, Joint charge storage for high-rate aqueous zinc-manganese dioxide

batteries, Adv. Mater. 31 (2019) 1900567.

[45] R. Zheng, C. Shu, Z. Hou, A. Hu, P. Hei, T. Yang, J. Li, R. Liang, J. Long, In situ fabricating oxygen vacancy-rich TiO_2 nanoparticles *via* utilizing thermodynamically metastable Ti atoms on $Ti_3C_2T_x$ MXene nanosheet surface to boost electrocatalytic activity for high-performance Li-O_2 batteries, ACS Appl. Mater. Inter. 11 (2019) 46696-46704.

[46] X. Han, Y. Huang, S. Gao, G. Zhang, T. Li, P. Liu, A hierarchical carbon fiber@MXene@ZnO core-sheath synergistic microstructure for efficient microwave absorption and photothermal conversion, Carbon 183 (2021) 872-883.

[47] X. Liang, C. Hart, Q. Pang, A. Garsuch, T. Weiss, L.F. Nazar, A highly efficient polysulfide mediator for lithium-sulfur batteries, Nat. Commun. 6 (2015) 5682.

[48] Z. Jin, C. Liu, Z. Liu, J. Han, Y. Fang, Y. Han, Y. Niu, Y. Wu, C. Sun, Y. Xu, Rational design of hydroxyl- rich $Ti_3C_2T_x$ MXene quantum dots for high- performance electrochemical N_2 reduction, Adv. Energy Mater. 10 (2020) 2000797.

[49] Q. Zhang, F. Wang, H. Zhang, Y. Zhang, M. Liu, Y. Liu, Universal Ti_3C_2 MXenes based self-standard ratiometric fluorescence resonance energy transfer platform for highly sensitive detection of exosomes, Anal. Chem. 90 (2018) 12737-12744.

[50] C.-F. Du, K.N. Dinh, Q. Liang, Y. Zheng, Y. Luo, J. Zhang, Q. Yan, Self-assemble and in situ formation of $Ni_{1-x}Fe_xPS_3$ nanomosaic-decorated MXene hybrids for overall water splitting, Adv. Energy Mater. 8 (2018) 1801127.

[51] H.-W. Wang, M. Naguib, K. Page, D.J. Wesolowski, Y. Gogotsi, Resolving the structure of $Ti_3C_2T_x$ MXenes through multilevel structural modeling of the atomic pair distribution function, Chem. Mater. 28 (2015) 349-359.

[52] F. Ye, L. Gong, Y. Long, S.N. Talapaneni, L. Zhang, Y. Xiao, D. Liu, C. Hu, L. Dai, Topological defect- rich carbon as a metal-free cathode catalyst for high-performance Li-CO_2 batteries, Adv. Energy Mater. 11 (2021) 2101390.

[53] Y. Shi, Y. Liu, Vacancy and N dopants facilitated Ti^{3+} sites activity in 3d $Ti_{3-x}C_2T_y$ MXene for electrochemical nitrogen fixation, Appl. Catal. B：Environ. 297 (2021) 120482.

[54] Y. Wang, Y.-Z. Zhang, D. Dubbink, J.E. ten Elshof, Inkjet printing of δ-MnO_2 nanosheets for flexible solid-state micro-supercapacitor, Nano Energy 49 (2018) 481-488.

[55] Z. Li, S. Ganapathy, Y. Xu, Q. Zhu, W. Chen, I. Kochetkov, C. George, L.F. Nazar, M. Wagemaker, Fe_2O_3 nanoparticle seed catalysts enhance cyclability on deep (dis)charge in aprotic Li-O_2 batteries, Advanced Energy Materials 8 (2018) 1703513.

[56] C. Zhang, A. Wang, L. Guo, J. Yi, J. Luo, A moisture-assisted rechargeable Mg-CO_2 battery, Angew. Chem., Int. Ed. (2022) 202200181.

[57] J. Wang, J.G. Wang, H. Liu, Z. You, Z. Li, F. Kang, B. Wei, A highly flexible and lightweight MnO_2/graphene membrane for superior zinc- ion batteries, Adv. Funct. Mater. 31 (2020) 2007397.

[58] X. Wang, F. Meng, Q. Jiang, W. Zhou, F. Jiang, T. Wang, X. Li, S. Li, Y. Lin, J. Xu, Simple layer-by-layer assembly method for simultaneously enhanced electrical conductivity and thermopower of PEDOT:PSS/ce-MoS_2 heterostructure films, ACS Appl. Energy Mater. 1 (2018) 3123-3133.

[59] S. Ghosh, S. Ganguly, S. Remanan, N.C. Das, Fabrication and investigation of 3D tuned PEG/PEDOT: PSS treated conductive and durable cotton fabric for superior electrical conductivity and flexible electromagnetic interference shielding, Compos. Sci. and Technol.

181 (2019) 107682.

[60] P. Wang, D. Zhao, X. Hui, Z. Qian, P. Zhang, Y. Ren, Y. Lin, Z. Zhang, L. Yin, Bifunctional catalytic activity guided by rich crystal defects in Ti_3C_2 MXene quantum dot clusters for Li-O_2 batteries, Adv. Energy Mater. 11 (2021) 2003069.

[61] J. Li, K. Han, J. Huang, G. Li, S. Peng, N. Li, J. Wang, W. Zhang, Y. Du, Y. Fan, W. Wang, F. Dang, Polarized nucleation and efficient decomposition of Li_2O_2 for Ti_2C MXene cathode catalyst under a mixed surface condition in lithium-oxygen batteries, Energy Storage Mater. 35 (2021) 669-678.

TOC

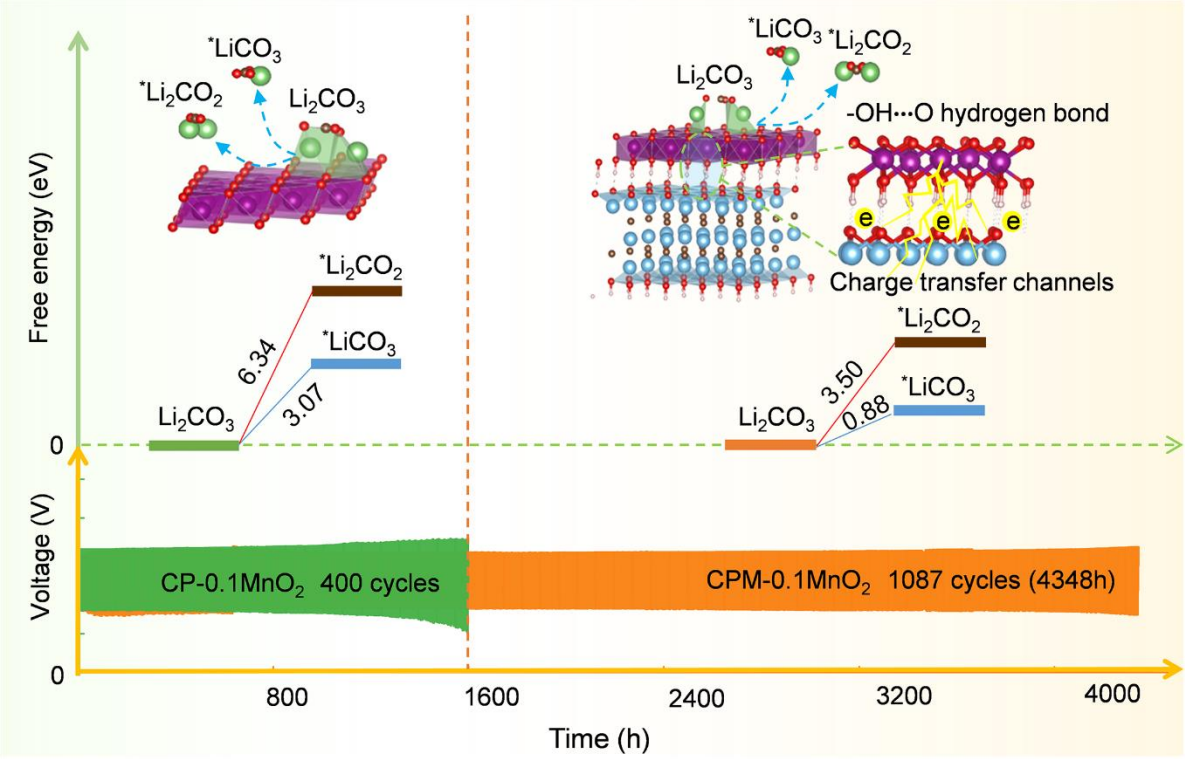

Strategies for changing the conductivity of Li_2CO_3 is introduced into the fabrication of Li-CO_2 battery. Benefitting from the favorable hierarchical architecture constructed (CPM-MnO_2), facile charge transfer occurs between catalytic surface and Li_2CO_3 by -OH···O hydrogen bonds improves the metallicity of Li_2CO_3, facilitating the formation/decomposition of Li_2CO_3 and bestowing an ultra-long-term stability of 1087 cycles (4348 h). Taking into account its simplicity, scalable character and outstanding performance, this hierarchical composite electrode paves an effective trajectory for the future development of highly efficient cathodes for durable metal-CO_2 batteries.

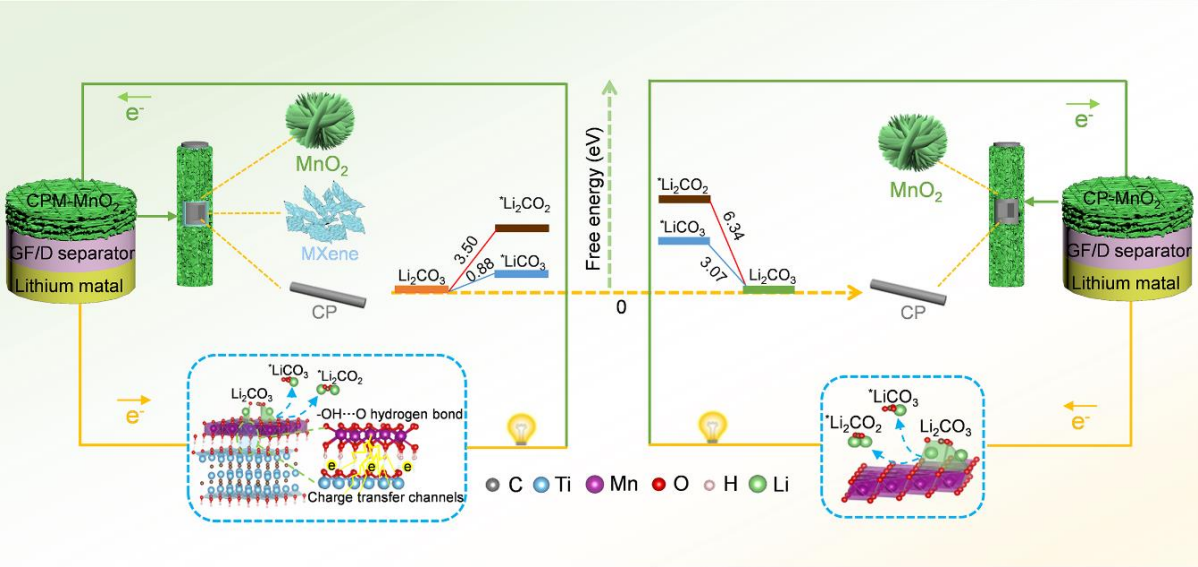

Scheme 1. Schematic illustration for the design and preparation of the integrated CPM-MnO_2 and CP-MnO_2 cathode, respectively.

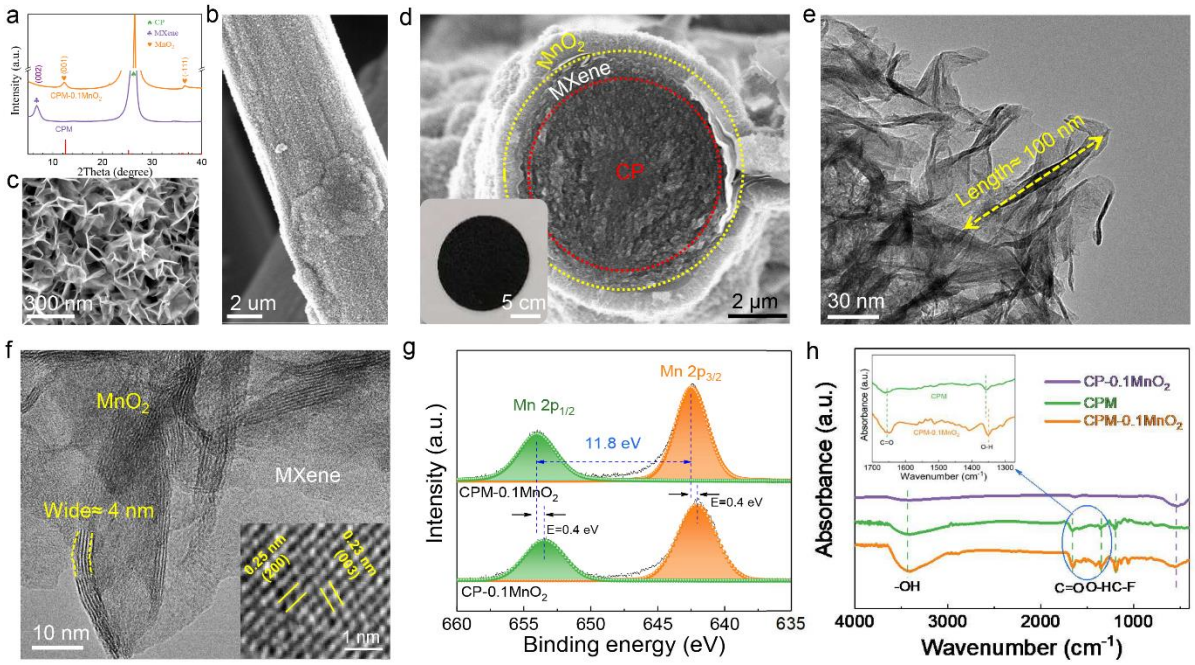

Fig. 1. Characterization of CP-MXene-MnO_2. a) XRD, b-d) SEM and e) TEM and f) HRTEM image of CPM-0.1MnO_2, respectively. The inside of d) is the digital photo and the inside of f) is HRTEM of MnO_2 in CPM-0.1MnO_2, respectively. g) XPS profiles of Mn 2p in CP-MnO_2 and CPM-0.1MnO_2, respectively. h) FTIR profiles of CP-0.1MnO2, CPM and CPM-0.1MnO_2, respectively.

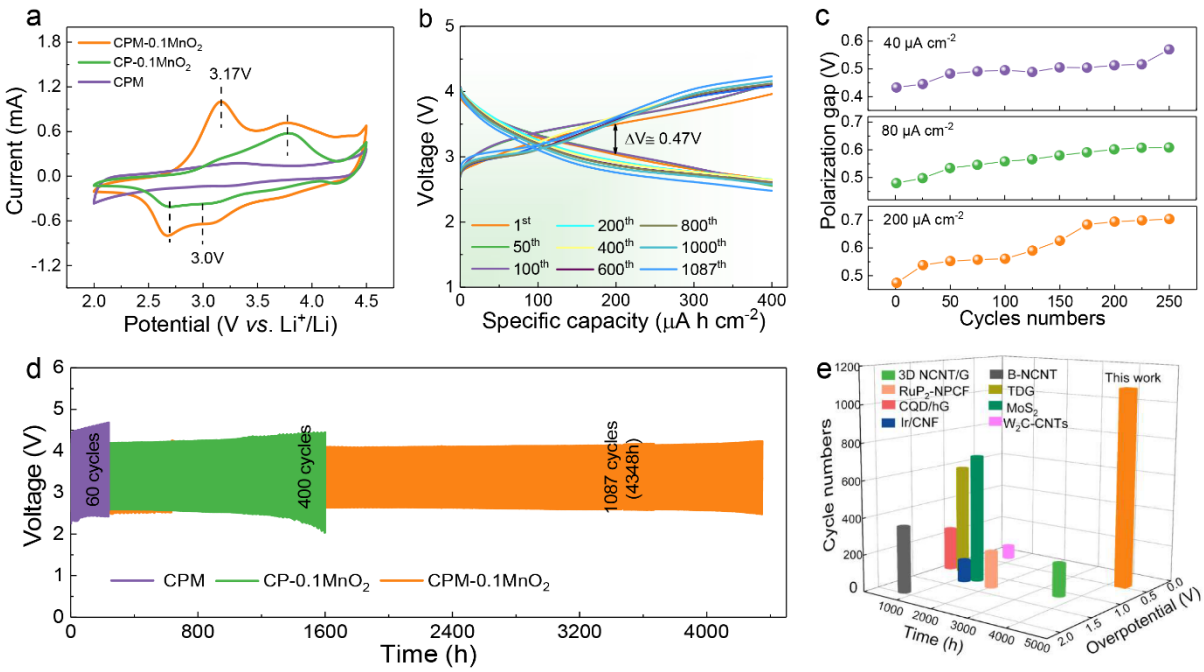

Fig. 2. a) CV curves of CPM, CP-0.1MnO_2 and CPM-0.1MnO_2 based batteries, the scan rate is 0.2 mVs^{-1}. b) Discharge-charge profiles of CPM-0.1MnO_2 Li-CO_2 batteries at different cycles. c) Polarization gap (V) for 400 μA h cm^{-2} capacity as a function of a number of cycles at different current densities. d) Comparison of time-voltage curves during the discharge-charge processes of the Li-CO_2 batteries with three different cathodes. e) Performance comparison with the previously reported results in terms of overpotential, cycle number and total operation time.

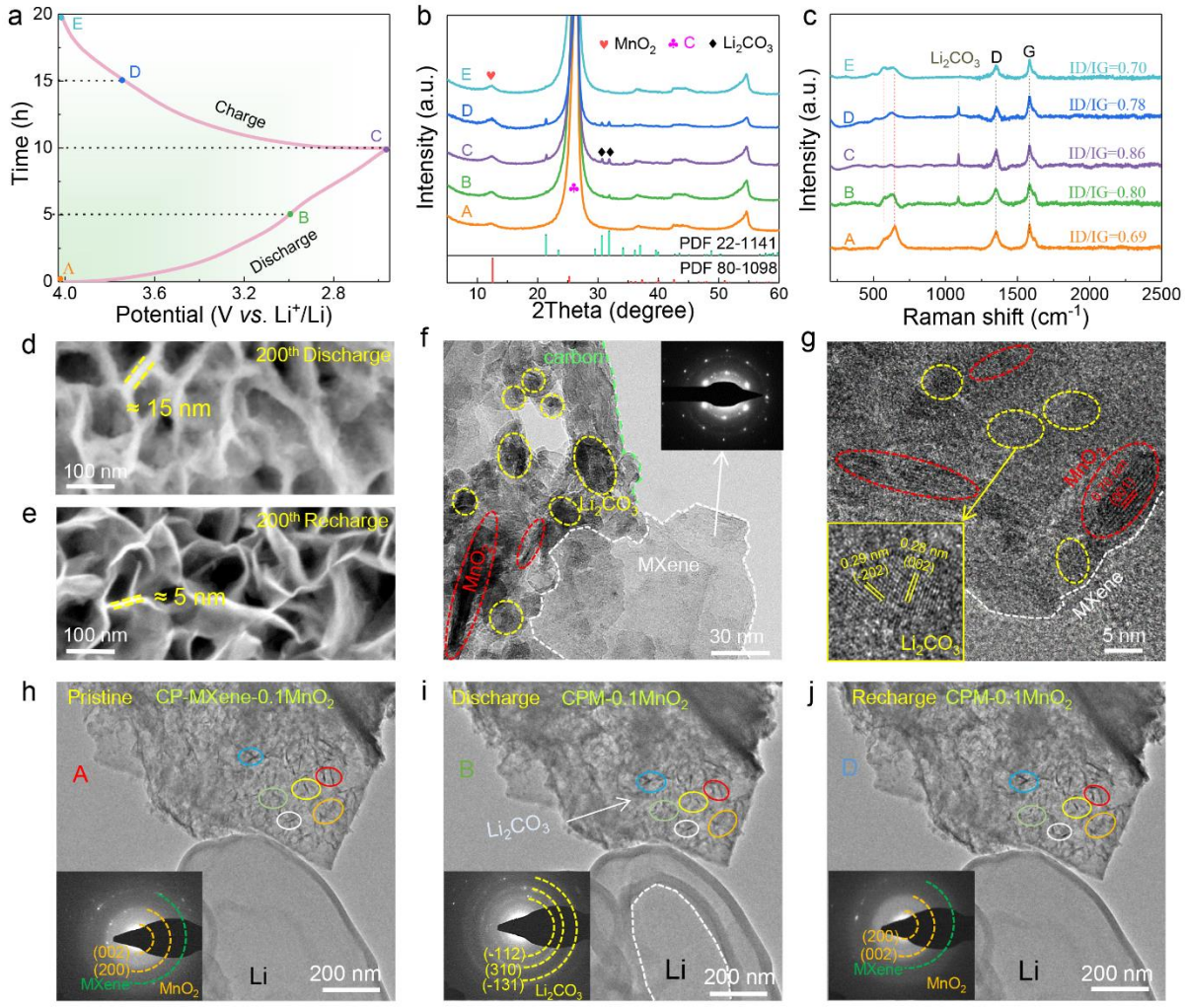

Fig. 3. The reaction process of CPM-0.1MnO_2-based Li-CO_2 battery. a) The galvanostatic discharge/charge profiles at a current density of 40 μA h cm^{-2}. b-c) *Ex-situ* XRD and Raman spectra at 5 selected points in one cycle. d) Discharge and e) charge processes about SEM image of cathode surface. f-g) TEM and HRTEM image of a discharged cathode sample. In situ microstructural features morphology variation of the CPM-0.1MnO_2 during the h) Pristine, i) Discharge and j) Recharge process. The inset is *In-situ* SAED patterns.

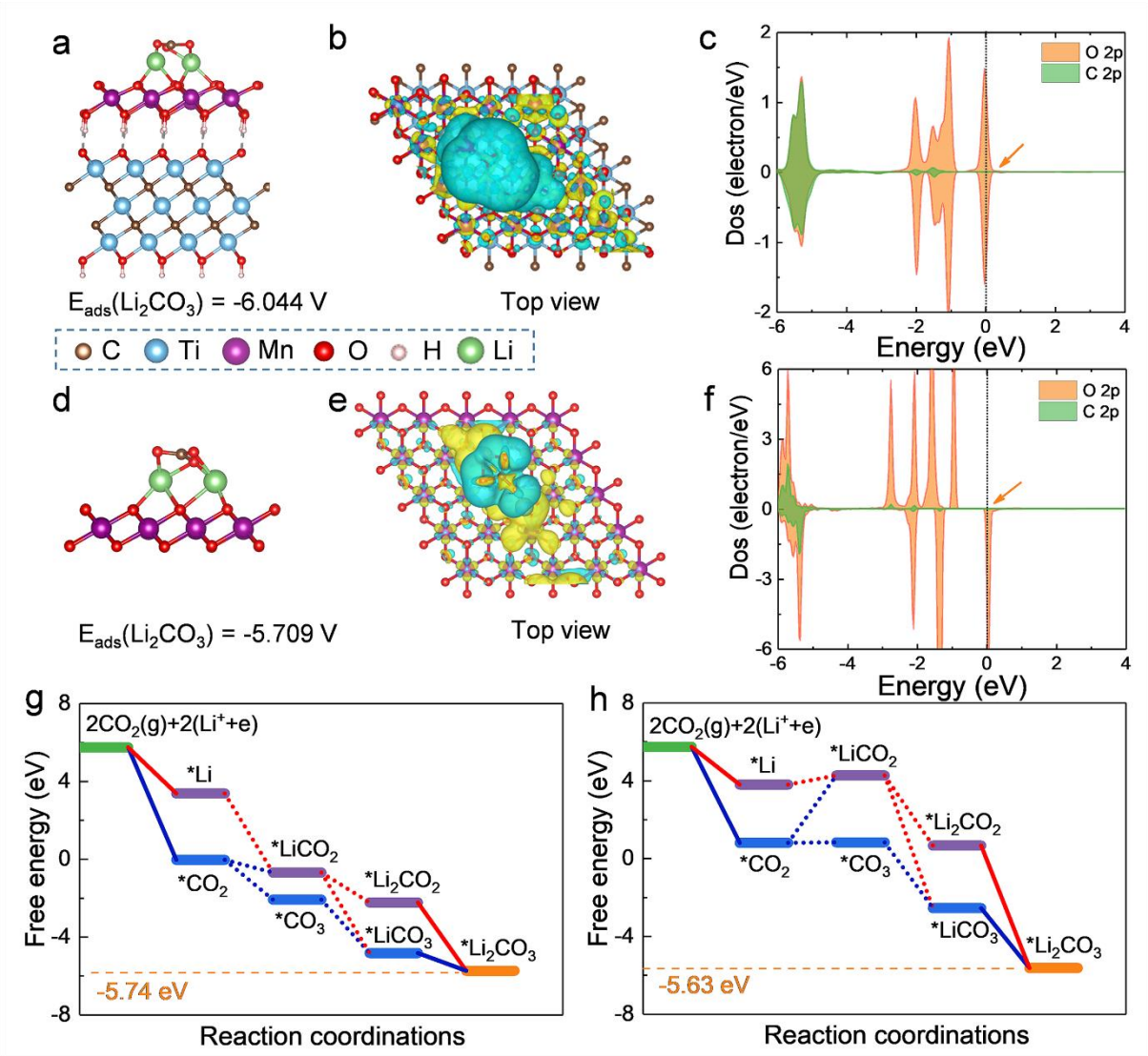

Fig. 4. DFT calculations and proposed mechanisms. Optimized structure and the corresponding binding energy of Li_2CO_3 on a) M-MnO_2 and d) MnO_2. Corresponding charge density distribution of Li_2CO_3 on b) M-MnO_2 and e) MnO_2. The DOS of Li_2CO_3 in c) M-MnO_2 and f) MnO_2, respectively. Calculated free energy diagrams for the different paths reactions on the active surface of g) M-MnO_2 and h) MnO_2.